Research Square

Preprints are preliminary reports that have not undergone peer review.
They should not be considered conclusive, used to inform clinical practice,
or referenced by the media as validated information.

Synthesizing antikekulene with global antiaromaticity and high stability

Xiaopeng Li

xiaopengli@sioc.ac.cn

Shanghai Institute of Organic Chemistry, Chinese Academy of Sciences https://orcid.org/0000-0001-9655-9551

Linyu Zhu

Shanghai Institute of Organic Chemistry, University of Chinese Academy of Sciences, Chinese Academy of Sciences https://orcid.org/0000-0003-1822-3221

Manting Mu

Institute of Physics, Czech Academy of Sciences

Minjian Liao

Shanghai Institute of Organic Chemistry, Chinese Academy of Sciences

Zihua Li

Shanghai Institute of Organic Chemistry, Chinese Academy of Sciences

Longnan Yu

Shanghai Institute of Organic Chemistry, Chinese Academy of Sciences

Xiaoxuan Su

Shanghai Institute of Organic Chemistry, Chinese Academy of Sciences

Haojun Xu

Shanghai Institute of Organic Chemistry, Chinese Academy of Sciences

Weijin Dai

Shanghai Institute of Organic Chemistry, Chinese Academy of Sciences

Yating Zhang

National Synchrotron Radiation Laboratory, University of Science and Technology of China

Yulun Wu

National Synchrotron Radiation Laboratory, University of Science and Technology of China

Hang Li

Shanghai Institute of Organic Chemistry, Chinese Academy of Sciences

Junfa Zhu

University of Science and Technology of China https://orcid.org/0000-0003-0888-4261

Heng Wang

Shanghai Institute of Organic Chemistry

Pavel Jelinek

Institute of Physics of the Czech Academy of Sciences, Cukrovarnická 10, 16200 Prague 6, Czech Republic https://orcid.org/0000-0002-5645-8542

Tao Wang

Shanghai Institute of Organic Chemistry, CAS https://orcid.org/0000-0002-6545-5028

Physical Sciences - Article

Keywords:

Posted Date: November 26th, 2026

DOI: https://doi.org/10.21203/rs.3.rs-11598609/v1

License: This work is licensed under a Creative Commons Attribution 4.0 International License. Read Full License

Additional Declarations: There is **NO** Competing Interest.

Abstract

Antiaromaticity is conventionally associated with intrinsic instability, posing a fundamental challenge to the synthesis and isolation of globally antiaromatic hydrocarbons. Most known examples have been realized either in ionic states or through heteroatom incorporation to relieve antiaromatic destabilization. Antikekulene (antiK), proposed by Vollhardt in 1986, is an iconic globally antiaromatic hydrocarbon comprising alternating benzene and cyclobutadiene rings whose inner and outer circuits both satisfy the 4n criterion. Extensive solution-phase efforts toward its synthesis have failed presumably owing to antiaromatic destabilization and/or severe skeletal strain. Theoretical studies have also debated whether antiaromaticity is the principal obstacle, and whether antiK can exist as a stable species is unresolved. Here we report surface-assisted synthesis of antiK on Ag(111) via dechlorination and doubly [2+2] cyclization of σ-radical intermediates stabilized by the surface and otherwise inaccessible in solution. Scanning probe methods and theoretical calculations reveal chemical and electronic structures associated with global antiaromaticity. Remarkably, antiK remains intact upon air exposure and can be extracted into solution for mass-spectrometric validation. It shows negligible oxidation after one week in air, opening avenues for future scalable synthesis. These results demonstrate that global antiaromaticity does not necessarily preclude molecular stability and establish a surface route to globally antiaromatic hydrocarbons.

Main

Aromaticity, one of the most fundamental concepts in chemistry, originates from cyclic delocalization of π electrons, leading to enhanced thermodynamic stability[16]. According to Hückel's rule, planar monocyclic conjugated systems bearing (4n+2) π electrons exhibit aromaticity with substantial resonance stabilization, whereas those with 4n π electrons suffer from antiaromatic destabilization[16,17]. Benzene and cyclobutadiene represent the classic examples of these two extremes (Fig. 1a). Benzene, with its exceptional aromatic stability, is readily isolable and has become a cornerstone of modern organic chemistry[18,19]. In stark contrast, cyclobutadiene is intrinsically unstable; even its Jahn-Teller distortion from D_{4h} to D_{2h} symmetry, which partially lifts orbital degeneracy, merely renders it a transient species observable only under cryogenic matrix conditions[20]. Over the past decades, expanding the boundaries of (anti)aromaticity to macrocyclic frameworks with global (anti)aromaticity has emerged as a central research theme in synthetic and theoretical chemistry[21-25].

Among the most iconic targets in this realm are kekulene and its conceptual counterpart antikekulene (antiK; Fig. 1a and Supplementary Fig. 1)[26]. Kekulene, often called superbenzene, contains concentric π-electron circuits that individually satisfy Hückel's (4n+2) criterion. Although its global aromaticity was disproved experimentally[27,28], the stabilization arising from local aromaticity enabled its successful synthesis as early as 1978 by Staab and Diederich[29]. AntiK, whose inner and outer π-electron circuits both satisfy the 4n criterion, is the representative hydrocarbon macrocycle for exploring the opposite limit of aromaticity[8]. It is also recognized as a subunit of graphenylene (Supplementary Fig. 2), a

potential semiconducting carbon allotrope first conceived by Balaban in 1968[30,31]. Vollhardt and coworkers devoted substantial pioneering efforts to the solution-phase synthesis of antiK[9-12], but all routes failed at the final ring-closing step (Supplementary Fig. 1), presumably reflecting the combined effects of global antiaromatic destabilization and the severe skeletal strain incurred during macrocycle closure. As a result, to the best of our knowledge, the synthesis of antiK has not been achieved previously and remained a theoretical molecule for forty years[26].

Here we report a surface-assisted approach for the synthesis of antiK via a doubly [2+2] cyclization reaction on an Ag(111) surface under ultrahigh-vacuum (UHV) conditions (Fig. 1b)[32,33]. Upon thermal activation, precursors AK-4Cl undergo complete dechlorination on Ag(111), generating surface-bound radical intermediates that undergo doubly [2+2] cyclizations to afford the antiK macrocycle. This strategy overcomes the challenges that have impeded previous solution-phase syntheses, where transition-metal-complex-catalyzed or ionic reaction pathways were unable to surmount the severe skeletal strain and steric congestion associated with macrocycle formation (Supplementary Fig. 1). The Ag(111) surface plays a dual role by promoting reactive dechlorinated carbon species that are passivated by the surface, while still preserving their reactivity to undergo C–C bond formation.

Surface-assisted synthesis of antiK

Scanning tunneling microscopy (STM) images of the sample prepared by depositing precursors AK-4Cl onto Ag(111) at 513 K show the formation of hexagonal macrocycles alongside several chain-like by-products (Fig. 2a,b). The bond-resolved (BR) STM and non-contact atomic force microscopy (nc-AFM) images acquired with a CO-functionalized probe (Fig. 2b,c) resolve the characteristic alternating six- and four-membered ring topology. The latter reveals distinct bond-order variations[34] in antiK, with stretched single bonds in the four-membered rings and alternating single and double bonds in the six-membered rings (Supplementary Fig. 3), consistent with previous theoretical predictions[8,35].

In addition to isolated molecules, extended, well-ordered hexagonal self-assembled domains of antiK were observed, with the largest molecular island accommodating approximately five hundred antiK units almost without defects (Fig. 2d,e). High-resolution STM images reveal that each antiK molecule is surrounded by twelve Cl adatoms released during dichlorination. These Cl adatoms aggregate antiK molecules into an ordered supramolecular assembly via non-covalent interactions (Supplementary Fig. 4). Together, STM images also reveal several by-products, most prominently C–Ag–C linked organometallic chains and ‘6-4’ chains (Fig. 2a,b). The predominant C–Ag–C species likely originate from cross-aligned radical intermediates that are stabilized by Ag adatoms following dechlorination (Fig. 2f and Supplementary Fig. 5). Statistical analysis (Supplementary Table 1) shows that the overall yield of antiK remains below 5%, with this value representing the highest yield obtained among the various deposition and annealing strategies we tested on a clean Ag(111) surface (Supplementary Figs. 6 and 8).

To gain further insight into the reaction pathway for the formation of antiK and by-products, we conducted synchrotron radiation photoelectron spectroscopy (SRPES) measurements to monitor the reaction progress. As shown in Fig. 3a, the Cl $2p_{3/2}$ peak assigned to intact precursor molecules (200.6 eV) attenuates from 373 K and disappears completely by 423 K, concomitant with the emergence of characteristic signals of Cl adatoms (small dots in Fig. 2a) on Ag(111) at 197.5 eV[36], revealing a broad temperature window of dechlorination. As C–Cl bond cleavage proceeds, the C–Ag spectral feature at a low binding energy (283.1 eV) intensifies during thermal annealing. At 423 K, the C–Ag component grows to ~10% of the total carbon species, which translates to a >50% proportion of C–Ag-containing products among all reaction products, consistent with the STM observations (Supplementary Fig. 6). In addition, these C–Ag bonded organometallic by-products persist even after complete C–Cl dissociation at 473 K (Supplementary Fig. 10), demonstrating their remarkable thermal stability.

To further elucidate the mechanism of antiK formation from AK-4Cl on Ag(111), density functional theory (DFT) calculations were performed (see Supplementary Information for computational details). Figure 3b shows the proposed reaction pathway for the formation of antiK, based on the DFT results, including the key intermediates and transition states (TSs). The competing pathways involving Ag coordination and trans-[2+2] cyclization are also indicated, with a more detailed discussion provided in the supplementary text. The reaction begins with surface-assisted C–Cl activation. Among the possible initial cleavage pathways, terminal dechlorination is favored with a Gibbs activation barrier of 1.59 eV (**TS1**), compared with 1.71 eV (**TS1b**, Supplementary Fig. 11) for bridging C–Cl cleavage. The resulting intermediate **I3** is also more stable than the corresponding bridging-dechlorinated species **I3b** (0.06 vs. 0.40 eV). Ag adatom-assisted dechlorination was found to be less favorable, with a barrier of 2.01 eV (**TS1'**, Supplementary Fig. 12), indicating that the initial C–Cl activation proceeds through direct surface-assisted dechlorination.

The monodechlorinated intermediate **I3** is stabilized through interaction with the Ag(111) surface via a direct C–Ag σ bond, with a calculated bond length of 2.2 Å. In contrast, the corresponding species in the gas phase or in solution would be a carbon-centered σ radical, which is intrinsically high in energy due to the unpaired electron occupying a low-lying σ orbital. Following formation of **I3**, the second dechlorination preferentially proceeds through cleavage of the bridging C–Cl bond on the same benzene ring, yielding **I5** with a barrier of 1.19 eV. Alternative pathways were considered but produce less stable intermediates (Supplementary Fig. 13). Further dechlorination of **I5** proceeds through a mirrored mechanism for the third and fourth dechlorination steps relative to the first and second steps, with activation barriers of 1.64 eV (**TS3**) and 0.87 eV (**TS4**), respectively (Supplementary Fig. 14). These sequential dechlorination events result in the formation of the tri- and tetra-dechlorinated intermediates **I7** and **I9**, respectively, through an overall exergonic process, with **I9** formation energy of −0.71 eV. Spin-polarized DFT calculations show no local magnetic moments on the reacting carbon atoms in **I9**. This is consistent with a closed-shell, surface-stabilized intermediate with a direct C–Ag σ bond rather than an open-shell radical species. The fully dechlorinated intermediate **I9** subsequently undergoes doubly cis-

[2+2] cyclization with an activation barrier of 0.17 eV (**TS5**, Supplementary Figs. 16 and 17) to yield antiK. Thus, the calculated reaction landscape supports a stepwise dechlorination pathway followed by facile cyclization as the mechanism responsible for antiK formation.

Comparing the on-surface UHV synthesis with solution-phase attempts, the Ag(111) surface provides a unique reaction environment in which the surface-quenched σ radical intermediates (**I3**, **I5**, **I7**, and **I9**) can be generated and stabilized long enough to undergo the subsequent surface-assisted dechlorination pathway and carbon bond formation. In contrast, the equivalent high-energy σ radical species are not stabilized and are more challenging to form in solution. This surface stabilization offers a tentative rationale for why the corresponding reaction has not been achieved in solution.

At the same time, however, the Ag(111) surface also introduces a competing pathway through Ag adatoms[37,38]. The experimentally observed major by-products, C–Ag–C species (Fig. 2f), are associated with Ag adatom binding to partially or fully dechlorinated intermediates (Fig. 3b). DFT calculations show that coordination of an Ag adatom to intermediate **I3** is energetically favorable by −0.25 eV (Supplementary Fig. 12). This alternative process disrupts the reaction pathway towards antiK and highlights the role of Ag adatoms in determining product selectivity. To limit the generation and diffusion of Ag adatoms, we introduced a pre-deposited Br layer on Ag(111). Experimentally, ~0.3 monolayer (ML) Br adatoms effectively passivate step edges (Supplementary Fig. 21a,b), which are considered major sources of Ag adatoms under reaction conditions (Supplementary Fig. 19). Under otherwise optimized deposition conditions, this Br-mediated strategy increases the antiK yield from <5% to ~30%, concomitant with substantial decreases in the C–Ag–C species (Supplementary Figs. 21 and 22, Supplementary Table 1). The calculated binding energy of an Ag adatom to the 0.3 ML Br-covered Ag(111) surface is favorable by –0.36 eV relative to the bare Ag(111) surface (Supplementary Fig. 20), supporting the role of Br in suppressing Ag-adatom diffusion.

Electronic structure of antiK

With the on-surface synthesis of antiK established and a reasonable yield achieved, the next question arises: does the metal surface play an active role in stabilizing this globally antiaromatic macrocycle? The observed product could represent either the desirable intact antiK or a molecule–substrate hybrid species strongly coupled to Ag(111)[39,40]. To address this, we performed nc-AFM frequency shift (Δf–z) spectroscopy to measure the adsorption height (Fig. 4a). The inner rim of antiK lies 3.13 Å above the Ag(111) surface, in close agreement with the theoretical value of 3.16 Å. This height is also comparable to the adsorption height of graphene on Ag(111)[41], suggesting a weak physical adsorption of antiK[40]. Moreover, both experiment and theory show that antiK remains essentially planar upon adsorption, with only a slight height difference of 15 pm between the inner and outer rims (Fig. 4a).

The weak coupling between antiK and the Ag(111) surface was further probed via characterization of the electronic structure. The computed projected density of states from isolated antiK and surface-adsorbed antiK confirms that the orbital alignment of antiK remains nearly unchanged upon surface adsorption,

with no apparent charge transfer or electronic hybridization with Ag surface states (Supplementary Figs. 23 and 24). The electronic structure of antiK on Ag(111) was experimentally measured by differential conductance (d*I*/d*V*) spectra, revealing a moderate transport gap of 2.5 eV between two resonant states located at −1.5 and 1.0 V, respectively (Fig. 4b). The spatial distributions of all resolved resonances in d*I*/d*V* spectra were visualized by associated energy mapping (Fig. 4c), which correlates with the simulated spectra based on Dyson orbitals[42] (Fig. 4d) that in this closer shell case are the same as one-electron molecular orbitals[43] (Supplementary Fig. 25). Moreover, the closed-shell character of the ground state for antiK on Ag(111) is confirmed by good agreement between the experimental and theoretical data (Fig. 4c,d and Supplementary Figs. 25 and 26).

We further investigated the antiaromatic character of antiK using theoretical calculations (Fig. 4e–g, and Supplementary Fig. 27). The four-membered rings, despite a slight elongation of their outer-rim bonds, exhibit anticlockwise ring-current patterns in the anisotropy of the induced current density (ACID) analysis, and their nucleus-independent chemical shifts (NICS) values are consistent with antiaromatic character. The π-only ACID analysis also indicates antiaromatic character in both the outer rim and the inner twelve-membered macrocycle, collectively supporting the global antiaromatic character of antiK as predicted previously[14]. The six-membered rings exhibit bond-length alternation (Fig. 4g), deviating from the bond-length equalization characteristic of benzene. This observation, together with the ACID and NICS analyses, suggests a non-aromatic character for these rings that accommodates the global antiaromatic character of antiK.

Stability of antiK

To test the stability, we first exposed antiK on Ag(111) to air for 30 min, followed by annealing under vacuum to remove adsorbed gases from the surface[44]; the molecules remained intact, with no detectable degradation or loss of molecular density (Fig. 5a,b). Given their weak adsorption on Ag(111), we further sought to transfer surface-synthesized antiK from Ag(111) into a solvent-dispersed state to evaluate its stability beyond the surface environment. A mass-spectrometric workflow for characterizing molecules grown on metallic substrates was developed (Fig. 5c). Following air exposure, antiK was transferred from Ag(111) into organic solvents by rinsing and sonication with tetrahydrofuran and chloroform (Supplementary Fig. 28). The extract was then concentrated, drop-cast onto a target plate, and dried at 323 K prior to Laser Desorption/Ionization Mass Spectrometry (LDI-MS) analysis (see **Methods** section for details). The entire procedure, from sample exposure to ambient air to MS analysis, was completed within approximately 4 h.

The resulting mass spectrum exhibits a signal at *m*/*z* 444.09 with the expected isotope pattern, corresponding to $C_{36}H_{12}$, which matches the molecular composition of antiK (Fig. 5d). A prominent signal at *m*/*z* 446.09 was also observed and assigned to $[C_{36}H_{14}]^{+\cdot}$. Its relative abundance versus the signal of $[C_{36}H_{12}]^{+\cdot}$ increased with enhanced laser energy (Supplementary Fig. 29), suggesting that it originates from laser-induced bond cleavage followed by hydrogen transfer from solvent residues, as

well documented in the ionization process in LDI and Matrix-Assisted Laser Desorption/Ionization (MALDI)[45,46]. The ratio of these two signals remained nearly constant across samples from different preparation batches, further supporting that the signal at *m*/*z* 446.09 is the ring-opening product of antiK induced by laser (Supplementary Fig. 30). Moreover, negligible signals attributable to oxidation products were detected, indicating that antiK remained largely intact during ambient exposure and solvent extraction (Supplementary Fig. 31). The extracted sample was stored in solvents and reanalyzed after one week showing similar spectrum as that acquired shortly after extraction (Fig. 5d and Supplementary Fig. 31). Together, these results demonstrate the high stability of antiK during solvent-mediated transfer and subsequent storage under ambient conditions, thus extending our understanding of stability boundaries in globally antiaromatic hydrocarbon macrocycles.

Outlook

The forty-year challenge of synthesizing antiK has been overcome through surface-assisted doubly [2+2] cyclization on Ag(111). This strategy provides a promising route to planar, globally antiaromatic macrocycles by circumventing the strain and steric barriers that hinder conventional solution-phase synthesis. Remarkably, the robust stability of antiK under ambient conditions demonstrates that global antiaromaticity does not necessarily preclude molecular stability, thus providing an opportunity for its bulk synthesis and further extension to 2D graphenylene via heterogeneous catalysis. Unlike the two sp^2-hybridized planar carbon allotropes synthesized to date, graphene and the biphenylene network[47], which are zero-gap (semi)metals, the corresponding 2D lattice derived from antiK has been predicted to be semiconducting with a finite band gap arising from its unique antiaromatic topology, rendering it promising for future electronic technologies[31].

Methods

On-surface synthesis

The synthesis of antiK combines solution-phase preparation of a robust, isolable carbon scaffold with final ring closure on the surface. The synthetic procedure for the precursor AK-4Cl is detailed in the Supplementary Information. On-surface experiments were performed under UHV conditions with a base pressure below 1×10^{-9} mbar. Ag(111) single crystals or Ag(111)/mica (MaTeck) were prepared by repeated cycles of Ar^+ ion sputtering and annealing at 850 K. The precursor AK-4Cl was thermally evaporated from a Kentax Knudsen-type evaporator maintained at 393–413 K and deposited under three sets of conditions: (i) onto substrates held at room temperature, followed by post-annealing at 433–583 K; (ii) directly onto clean substrates held at elevated temperatures of 433–583 K; or (iii) onto Br-precovered Ag(111) substrates held at elevated temperatures of 513–558 K. Br-precovered Ag(111) surfaces were prepared by depositing 1,2,5,6-tetrabromocyclooctane onto Ag(111) held at 373 K, where the organic fragments desorbed, leaving Br adatoms on the surface.

STM and nc-AFM measurements

STM and AFM measurements were performed using a POLAR XT SPM system (Omicron) equipped with Nanonis control electronics. All measurements were conducted at approximately 4.4 K under UHV conditions, with a base pressure below 5×10^{-10} mbar. STM images were acquired using an etched W tip, while nc-AFM measurements were performed using an etched W tip mounted on a qPlus tuning-fork sensor. The sensor had a resonance frequency of f_0 = 26026 Hz and a quality factor of Q = 68400. nc-AFM images were acquired with an oscillation amplitude of A_{osc} = 180 pm at a bias voltage of U = 10 mV. For Δf–z spectroscopy, the oscillation amplitude was set to 40 pm and the bias voltage to 5 mV. The initial tip–sample distance was established at a set-point I = 20 pA, U = 5 mV. The tip was then first retracted by 200 pm and subsequently approached toward the sample by 300~500 pm while recording the frequency-shift response as a function of tip–sample distance. Differential conductance (dI/dV) measurements were performed using a lock-in amplifier with a bias modulation frequency of 773 Hz and a modulation amplitude of 20 mV. CO-terminated tips were used for bond-resolved imaging, Δf–z spectroscopy, and dI/dV measurements. STM and nc-AFM images were processed using WSxM software[48].

SRPES measurements

SRPES experiments were performed at the Catalysis and Surface Science Endstation of the National Synchrotron Radiation Laboratory (Hefei, China). Photoelectrons were collected at an emission angle of 45° relative to the surface normal. Cl 2*p* and C 1*s* spectra were sequentially collected from on-surface synthesis samples prepared by deposition of AK-4Cl on Ag(111) held at RT and subsequent annealing to different temperatures. After each annealing step, the sample was cooled to RT before SRPES measurement. Both Cl 2*p* and C 1*s* spectra were acquired with a photon energy of 350 eV.

Stability tests and mass spectrometric characterization

For the air-stability test, a sample was transferred to the fast-entry load-lock chamber and exposed to ambient conditions (298 K, relative humidity of approximately 40%) for 30 min by venting the chamber. The chamber was then re-evacuated, and the sample was annealed at 515 K for 20 min, followed by 538 K for 10 min, before STM characterization[44].

For solution-phase stability assessment and mass spectrometric characterization, surface-grown antiK on 1 cm × 1 cm Ag(111)/mica substrates (estimated to yield picogram-scale quantities) was extracted using organic solvents. After removal from the UHV chamber, the samples were handled under ambient conditions. The Ag(111) substrates were sequentially rinsed with THF and $CHCl_3$ (1.0 mL each), followed by immersion in each solvent and sonication for 5 min (Supplementary Fig. 28). All extracts were combined and concentrated to approximately 20 μL by rotary evaporation in a 313 K water bath. The concentrated extracts were deposited into the wells of a target plate and dried in a vacuum oven at 323 K for 30 min to remove residual solvents. The interval from removal of the samples from the UHV chamber to completion of sample preparation was approximately 4 h, during which the extracted material remained in the solvent-dispersed state until deposition onto the target plate. LDI-MS

measurements were performed in positive-ion reflectron mode using a Bruker Rapiflex MALDI-TOF mass spectrometer (Bruker Daltonics, Inc.) equipped with a 355 nm Nd laser.

Theoretical calculations

Periodic density functional theory (DFT) calculations were performed using GPAW[49] with the PBE exchange-correlation functional[50], Grimme's D3 dispersion correction with Becke-Johnson damping[51], and the projector augmented-wave method[52]. Surface reaction pathways for antiK formation, including on-surface dechlorination and [2+2] cyclization, were investigated using a 3-layer Ag(111) slab with a 6 × 6 supercell and K-point spacing of 0.025 2π $Å^{-1}$. Transition states were determined using the climbing-image nudged elastic band (CI-NEB) method[53]. Gibbs energy corrections at 523.15 K were calculated by including vibrational contributions within the harmonic approximation[54]. The multireference complete active space configuration interaction (CASCI) calculations were performed to further assess the ground-state electronic structure of antiK[55]. Aromaticity and induced ring-current characteristics were investigated using nucleus-independent chemical shifts (NICS)[56] and anisotropy of the induced current density (ACID) analyses[57].

48. Horcas, I. *et al.* WSXM: A software for scanning probe microscopy and a tool for nanotechnology. *Rev. Sci. Instrum.* **78**, 013705 (2007).
49. Mortensen, J. J. *et al.* GPAW: An open Python package for electronic structure calculations. *J. Chem. Phys.* **160**, 092503 (2024).
50. Perdew, J. P., Burke, K. & Ernzerhof, M. Generalized gradient approximation made simple. *Phys. Rev. Lett.* **77**, 3865-3868 (1996).
51. Grimme, S., Ehrlich, S. & Goerigk, L. Effect of the damping function in dispersion corrected density functional theory. *J. Comput. Chem.* **32**, 1456-1465 (2011).
52. Blöchl, P. E. Projector augmented-wave method. *Phys. Rev. B* **50**, 17953-17979 (1994).
53. Henkelman, G., Uberuaga, B. P. & Jónsson, H. A climbing image nudged elastic band method for finding saddle points and minimum energy paths. *J. Chem. Phys.* **113**, 9901-9904 (2000).
54. Grimme, S. Supramolecular binding thermodynamics by dispersion-corrected density functional theory. *Chem. Eur. J.* **18**, 9955-9964 (2012).
55. Roos, B. O. in *Advances in Chemical Physics* Vol. 69 399-445 (1987).
56. Chen, Z. F., Wannere, C. S., Corminboeuf, C., Puchta, R. & Schleyer, P. V. Nucleus-independent chemical shifts (NICS) as an aromaticity criterion. *Chem. Rev.* **105**, 3842-3888 (2005).
57. Geuenich, D., Hess, K., Köhler, F. & Herges, R. Anisotropy of the induced current density (ACID), a general method to quantify and visualize electronic delocalization. *Chem. Rev.* **105**, 3758-3772 (2005).

Declarations

Data availability

The data that support the findings of this study are available within the paper and the Supplementary Information. The Cartesian coordinates of the computed structures are accessible via the following Zenodo online dataset: DOI (to be added after acceptance of the manuscript). Any other relevant data are available from the corresponding authors on request.

Acknowledgments The authors gratefully acknowledge the DJEI/DES/SFI/HEA Irish Centre for High-End Computing (ICHEC) and the e-INFRA CZ project (ID: 90254) supported by the Ministry of Education, Youth and Sports of the Czech Republic (MEYS CR), for providing computational resources and support. This work was supported by Strategic Priority Research Program of the Chinese Academy of Sciences (XDB1180000), the National Natural Science Foundation of China (22574169 to H.L.; 22272157 to J.Z.; 22572213 to T.W.; 22125106 to X.L.), CzechNanoLab Research Infrastructure supported by MEYS CR (LM2023051) and the Czech Science Foundation project no. 25-17866X (P. J. and M.M).

Author Contributions T.W. and X.L. conceived and designed the experiments. M.L. and X.S. synthesized the precursor molecule and performed associated characterizations under the supervision of H.W. and X.L. L.Z., Z.L., L.Y., H.X., W.D., and T.W. conducted on-surface synthesis and associated STM/AFM measurements. Y.Z., Y.W., and L.Y. performed the SRPES measurements under the supervision of J.Z. M.L., L.Z., H.W., T.W., and X.L. performed the MS experiments. M.M. carried out the computational studies under the supervision of P.J. L.Z., M.M., H.L., and T.W. made the figures. L.Z., M.M., P.J., T.W., and X.L. co-wrote the paper. All authors discussed the results and commented on the manuscript at all stages.

Competing interests The authors declare no competing interests.

Additional information

Supplementary Information is available for this paper.

Correspondence and requests for materials should be addressed to Pavel Jelínek, Tao Wang, or Xiaopeng Li.

Peer review information includes the names of reviewers who agree to be cited and is completed by Nature staff during proofing.

Reprints and permissions information is available at www.nature.com/reprints.

References

1. Gao, Y. *et al.* On-surface synthesis of a doubly anti-aromatic carbon allotrope. *Nature* **623**, 977-981 (2023).

2. Sun, L. *et al.* On-surface synthesis and characterization of anti-aromatic cyclo[12]carbon and cyclo[20]carbon. *Nat. Commun.* **15**, 7649 (2024).
3. Peeks, M. D., Claridge, T. D. W. & Anderson, H. L. Aromatic and antiaromatic ring currents in a molecular nanoring. *Nature* **541**, 200-203 (2017).
4. Stawski, W. *et al.* The anti-aromatic dianion and aromatic tetraanion of [18]annulene. *Nat. Chem.* **16**, 998-1002 (2024).
5. Zhu, C. *et al.* Stabilization of anti-aromatic and strained five-membered rings with a transition metal. *Nat. Chem.* **5**, 698-703 (2013).
6. Ishida, M. *et al.* Protonation-coupled redox reactions in planar antiaromatic meso-pentafluorophenyl-substituted o-phenylene-bridged annulated rosarins. *Nat. Chem.* **5**, 15-20 (2013).
7. Yonezawa, T., Shafie, S. A., Hiroto, S. & Shinokubo, H. Shaping antiaromatic π-systems by metalation: Synthesis of a bowl-shaped antiaromatic palladium norcorrole. *Angew. Chem. Int. Ed.* **56**, 11822-11825 (2017).
8. Diercks, R. & Vollhardt, K. P. C. Novel synthesis of the angular [3]phenylene (terphenylene) by cobalt-catalyzed cyclization of bis(2-ethynylphenyl)ethyne: A molecule with an internal cyclohexatriene ring. *Angew. Chem. Int. Ed.* **25**, 266-268 (1986).
9. Eickmeier, C. *et al.* 5,6,11,12,17,18-Hexadehydro-1,4,7,10,13,16-hexaethynyltribenzo[a,e,i]cyclododecene: Synthesis and CpCo-catalyzed cycloisomerization to the first superdelocalized oligophenylenes. *Angew. Chem. Int. Ed.* **36**, 2103-2108 (1997).
10. Han, S. *et al.* Total syntheses and structures of angular [6]- and [7]phenylene: The first helical phenylenes (heliphenes). *Angew. Chem. Int. Ed.* **41**, 3223-3227 (2002).
11. Fonari, A., Röder, J. C., Shen, H., Timofeeva, T. V. & Vollhardt, K. P. C. Toward antikekulene: Angular 1,2-di-, 2,3-di-, and 1,2,15,16-tetrachloro[6]phenylene. *Synlett* **25**, 2429-2433 (2014).
12. Dahlmann, U. & Vollhardt, K. P. C. Oligoether-substituted derivatives of carbon-rich 1,4,7,10,13,16-hexaethynyltribenzo[a,e,i]cyclododeca-5,11,17-triyne (C36H12) and 1,4,9,12-tetrakis(ethynyl)dibenzo[a,g] cyclododeca-5,7,13,15-tetrayne (C28H8): Potential precursors to the circular [6]phenylene ('antikekulene') frame. *Synthesis* **52**, 1287-1300 (2020).
13. Babic, D. & Trinajstic, N. Kekulene and antikekulene. *J. Mol. Struct. THEOCHEM* **120**, 321-327 (1994).
14. Aihara, J.-i. A simple method for estimating the superaromatic stabilization energy of a super-ring molecule. *J. Phys. Chem. A* **112**, 4382-4385 (2008).
15. Prabhu, S., Arulperumjothi, M., Manimozhi, V. & Balasubramanian, K. Topological characterizations on hexagonal and rectangular tessellations of antikekulenes and its computed spectral, nuclear magnetic resonance and electron spin resonance characterizations. *Int. J. Quantum Chem.* **124**, e27365 (2024).
16. Breslow, R. Aromatic character. *Chem. Eng. News* **43**, 90-100 (1965).
17. Hückel, E. Quantentheoretische beiträge zum benzolproblem. *Z. Physik* **70**, 204-286 (1931).

18. Faraday, M. On new compounds of carbon and hydrogen, and on certain other products obtained during the decomposition of oil by heat. *Phil. Trans. R. Soc.* **115**, 440-466 (1825).
19. Kekulé, A. Sur la constitution des substances aromatiques. *Bull. Soc. Chim. Paris* **3**, 98-110 (1865).
20. Bally, T. & Masamune, S. Cyclobutadiene *Tetrahedron* **36**, 343-370 (1980).
21. Zeng, Z. *et al.* Pro-aromatic and anti-aromatic π-conjugated molecules: An irresistible wish to be diradicals. *Chem. Soc. Rev.* **44**, 6578-6596 (2015).
22. Rodríguez-Rubio, A. *et al.* Synthesis of triple stranded porphyrin nanobelts. *Science* **390**, 290-293 (2025).
23. Xu, B. *et al.* Metal-centred planar [15]annulenes. *Nature* **641**, 106-111 (2025).
24. Liu, C. *et al.* Macrocyclic polyradicaloids with unusual super-ring structure and global aromaticity. *Chem* **4**, 1586-1595 (2018).
25. Xiang, F. *et al.* Planar π-extended cycloparaphenylenes featuring an all-armchair edge topology. *Nat. Chem.* **14**, 871-876 (2022).
26. Miyoshi, H., Nobusue, S., Shimizu, A. & Tobe, Y. Non-alternant non-benzenoid kekulenes: The birth of a new kekulene family. *Chem. Soc. Rev.* **44**, 6560-6577 (2015).
27. Pozo, I. *et al.* Revisiting kekulene: Synthesis and single-molecule imaging. *J. Am. Chem. Soc.* **141**, 15488-15493 (2019).
28. Haags, A. *et al.* Kekulene: On-surface synthesis, orbital structure, and aromatic stabilization. *ACS Nano* **14**, 15766-15775 (2020).
29. Diederich, F. & Staab, H. A. Benzenoid versus annulenoid aromaticity: Synthesis and properties of kekulene. *Angew. Chem. Int. Ed.* **17**, 372-374 (1978).
30. Bally, I. *et al.* Chemical graphs. VI. Estimation of the relative stability of several planar and tridimensional lattices for elementary carbon. *Rev. Roum. Chim.* **13**, 231-247 (1968).
31. Brunetto, G. *et al.* Nonzero gap two-dimensional carbon allotrope from porous graphene. *J. Phys. Chem. C* **116**, 12810-12813 (2012).
32. Fan, Q., Gottfried, J. M. & Zhu, J. Surface-catalyzed C–C covalent coupling strategies toward the synthesis of low-dimensional carbon-based nanostructures. *Acc. Chem. Res.* **48**, 2484-2494 (2015).
33. Clair, S. & de Oteyza, D. G. Controlling a chemical coupling reaction on a surface: Tools and strategies for on-surface synthesis. *Chem. Rev.* **119**, 4717-4776 (2019).
34. Gross, L. *et al.* Bond-order discrimination by atomic force microscopy. *Science* **337**, 1326-1329 (2012).
35. Schulman, J. M. & Disch, R. L. Theoretical studies of the [N]phenylenes. *J. Am. Chem. Soc.* **118**, 8470-8474 (1996).
36. Dai, J. *et al.* Dechlorinated ullmann coupling reaction of aryl chlorides on Ag(111): A combined STM and XPS study. *Chemphyschem* **20**, 2367-2375 (2019).
37. Björk, J. *et al.* The role of metal adatoms in a surface-assisted cyclodehydrogenation reaction on a gold surface. *Angew. Chem. Int. Ed.* **61**, e202212354 (2022).

38. Mendieta-Moreno, J. I. *et al.* Unusual scaffold rearrangement in polyaromatic hydrocarbons driven by concerted action of single gold atoms on a gold surface. *Angew. Chem. Int. Ed.* **61**, e202208010 (2022).
39. Qie, B. *et al.* Synthesis and characterization of low-dimensional N-heterocyclic carbene lattices. *Science* **384**, 895-901 (2024).
40. Klein, B. P. *et al.* Molecular topology and the surface chemical bond: Alternant versus nonalternant aromatic systems as functional structural elements. *Phys. Rev. X* **9**, 011030 (2019).
41. Fukaya, Y., Entani, S. & Sakai, S. Reversible structure change in graphene/metal interface by intercalation and deintercalation. *Phys. Rev. B* **108**, 155422 (2023).
42. Ortiz, J. V. Dyson-orbital concepts for description of electrons in molecules. *J. Chem. Phys.* **153**, 070902 (2020).
43. Kumar, M. *et al.* Multireference theory of scanning tunneling spectroscopy beyond one-electron molecular orbitals: Can we image molecular orbitals? *J. Am. Chem. Soc.* **147**, 24993-25003 (2025).
44. Lawrence, J. *et al.* Circumventing the stability problems of graphene nanoribbon zigzag edges. *Nat. Chem.* **14**, 1451-1458 (2022).
45. Yamagaki, T. & Nobuhara, M. Structural categorization of adenine, guanine, and xanthine derivatives using matrix-assisted laser desorption/ionization mass spectrometry with 5-nitrosalicylic acid and 1,5-diaminonaphtalene. *J. Am. Soc. Mass. Spectrom.* **36**, 329-339 (2025).
46. Calba, P. J., Muller, J. F. & Inouye, M. H-atom transfer following analyte photoionization in matrix-assisted laser desorption/ionization processes. *Rapid Communications in Mass Spectrometry* **12**, 1727-1731 (1998).
47. Fan, Q. T. *et al.* Biphenylene network: A nonbenzenoid carbon allotrope. *Science* **372**, 852-856 (2021).

Figures

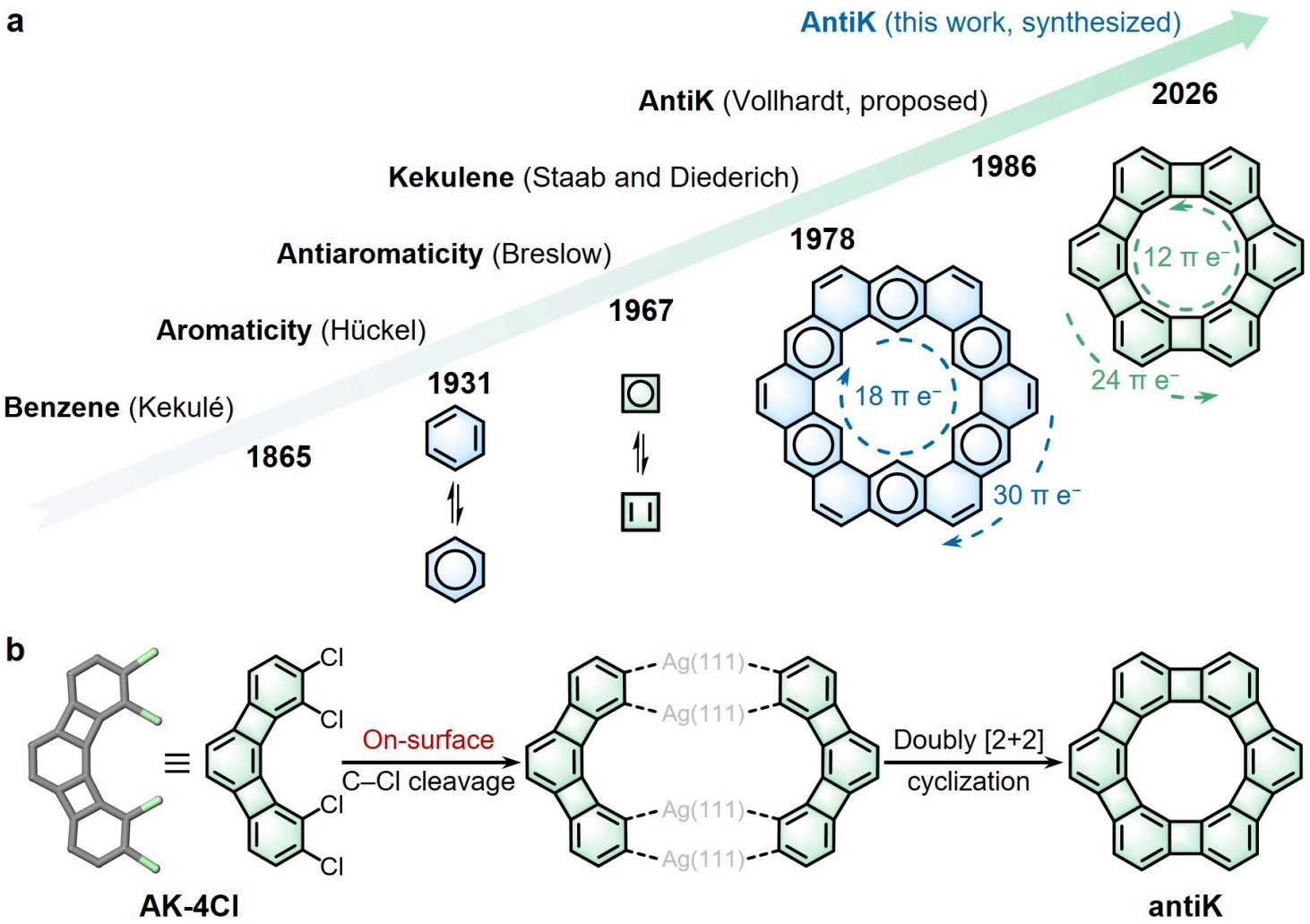

Figure 1

Introduction and synthesis of antiK. a, Timeline of the proposal and synthesis of iconic aromatic and antiaromatic hydrocarbons, including benzene, cyclobutadiene, kekulene, and antiK. **b**, On-surface synthesis of antiK on Ag(111), including complete dechlorination of AK-4Cl followed by doubly [2+2] cyclization. The precursor AK-4Cl was synthesized through a solution-phase route (see Supplementary Information).

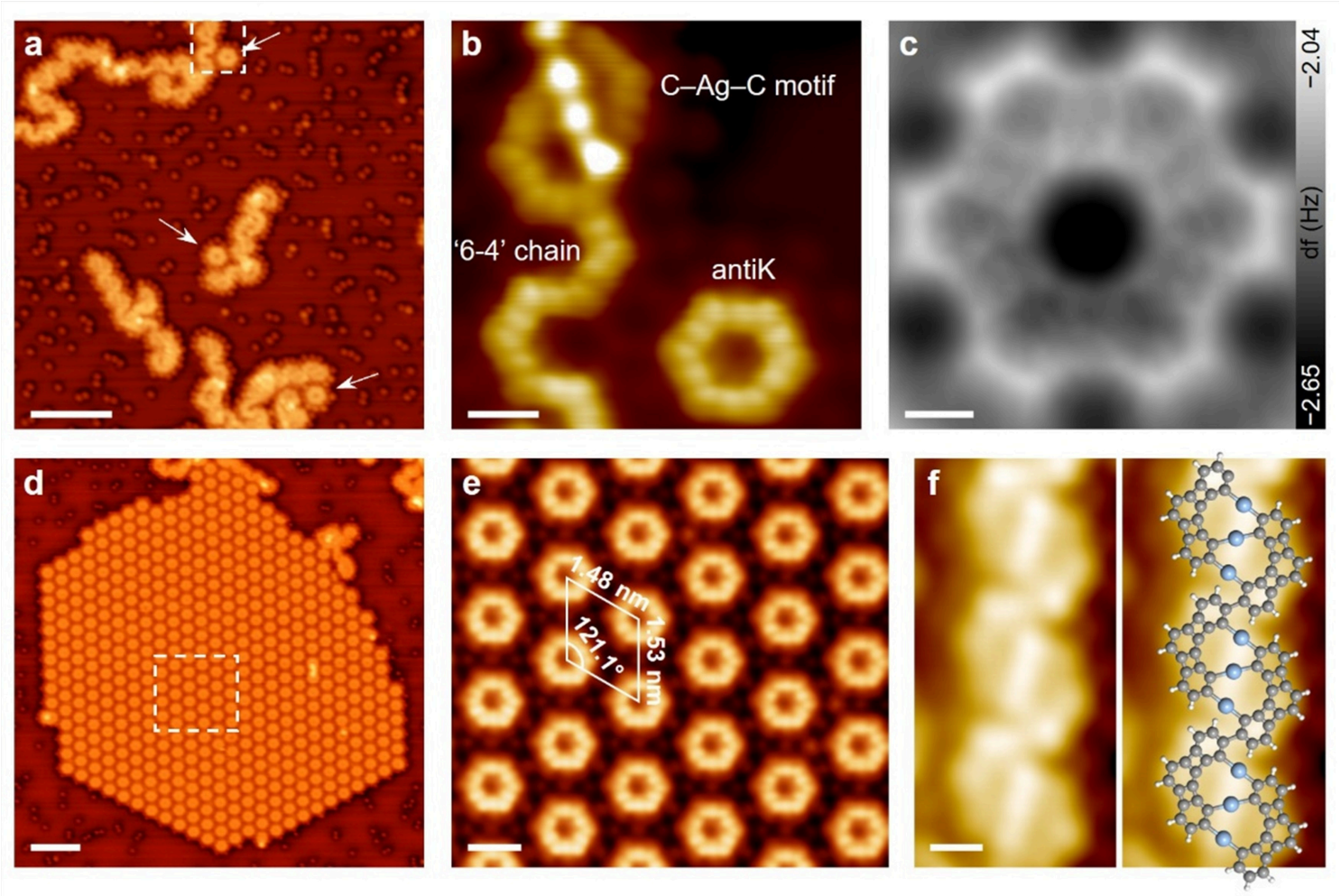

Figure 2

STM and nc-AFM imaging of antiK and major by-products on Ag(111). a, Representative STM image of the sample prepared by depositing AK-4Cl onto an Ag(111) surface held at 513 K. AntiK molecules are highlighted with white arrows. The small dots correspond to Cl adatoms adsorbing on the Ag(111) surface after dechlorination of AK-4Cl. **b**, Zoom-in BR-STM image of the dashed rectangular region in panel (**a**), presenting antiK and major by-products, including a C–Ag–C motif and a '6-4' chain. **c**, Experimental nc-AFM image of antiK acquired with a CO-functionalized tip. **d**, STM images of a hexagonal superlattice assembled by antiK molecules on the same sample. **e**, Zoom-in BR-STM image of the dashed rectangular region in panel (**d**). A unit cell of the supramolecular network is overlaid. **f**, STM image of a representative C–Ag–C linked organometallic chain, overlaid by its structural model. Scale bars, 5 nm (**a**,**d**), 0.5 nm (**b**,**f**), 0.2 nm (**c**), 1 nm (**e**). The Ag, C, and H atoms in the render are color-coded with light blue, grey, and white, respectively.

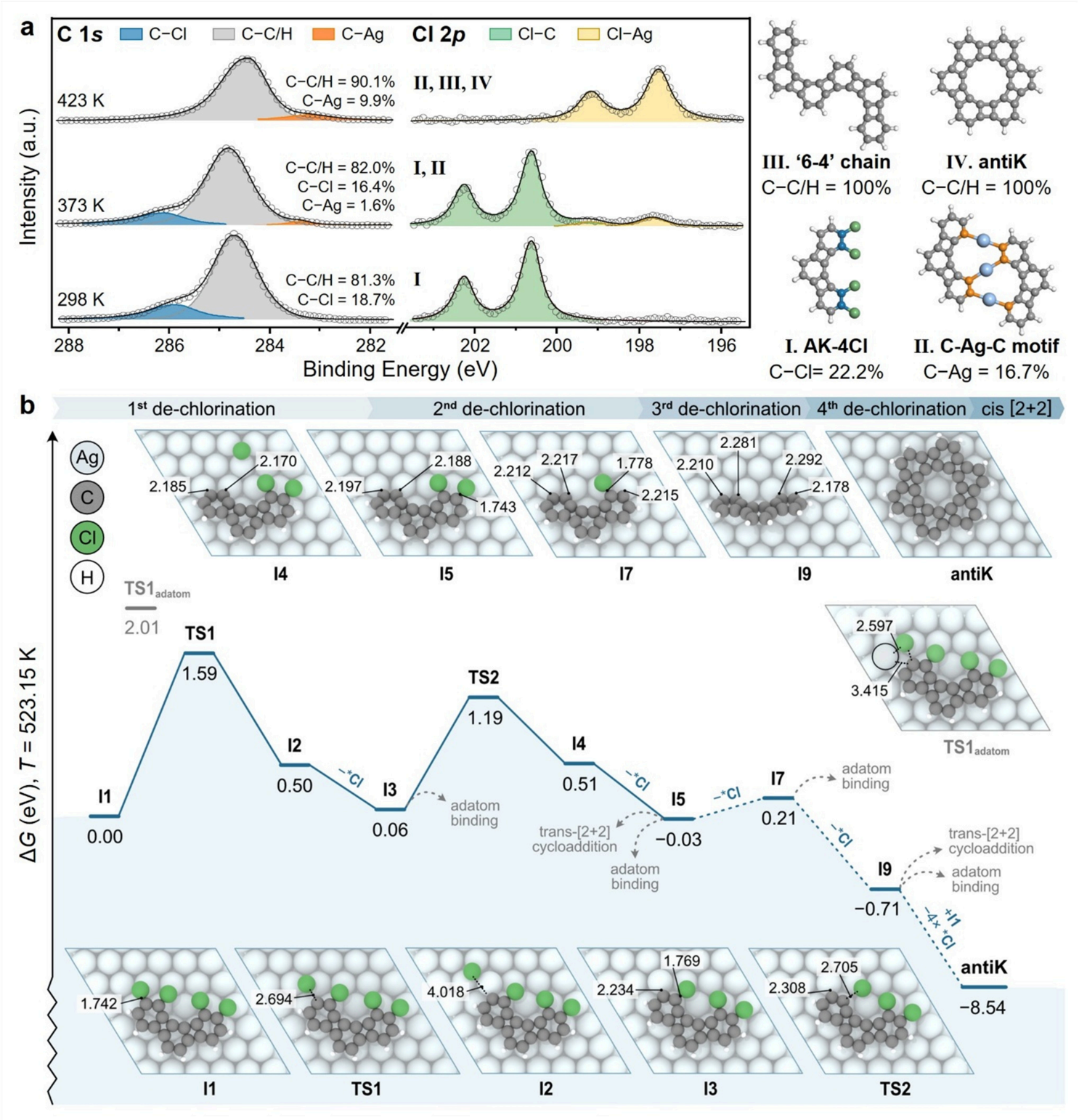

Figure 3

Mechanistic insights into antiK synthesis. a, SRPES for the C 1*s* and Cl 2*p* core levels (photon energy: 350 eV) acquired upon annealing AK-4Cl precursors on Ag(111) at the indicated temperatures, revealing the progressive dechlorination and generation of C–Ag–C species. Structural models of AK-4Cl and the three major products are shown on the right; carbon atoms with distinct chemical environments are color-coded, and their relative proportions in each structure are indicated. The relative contributions of

the different carbon species at each annealing stage are listed in the spectra, alongside the representative products denoted by Roman numerals. **b**, Gibbs energy profile for the dechlorination steps and subsequent cis-[2+2] cyclization leading to antiK formation. Energies are reported in eV at 523.15 K in vacuum. Alternative dechlorination pathways involving different C–Cl cleavage sites, as well as proposed pathways for by-product formation including Ag adatom coordination towards C–Ag–C linked organometallic species and trans-[2+2] cyclization towards '6-4' chains, are indicated in grey. The structures of key intermediates and TSs are shown, with selected bond distances given in Å.

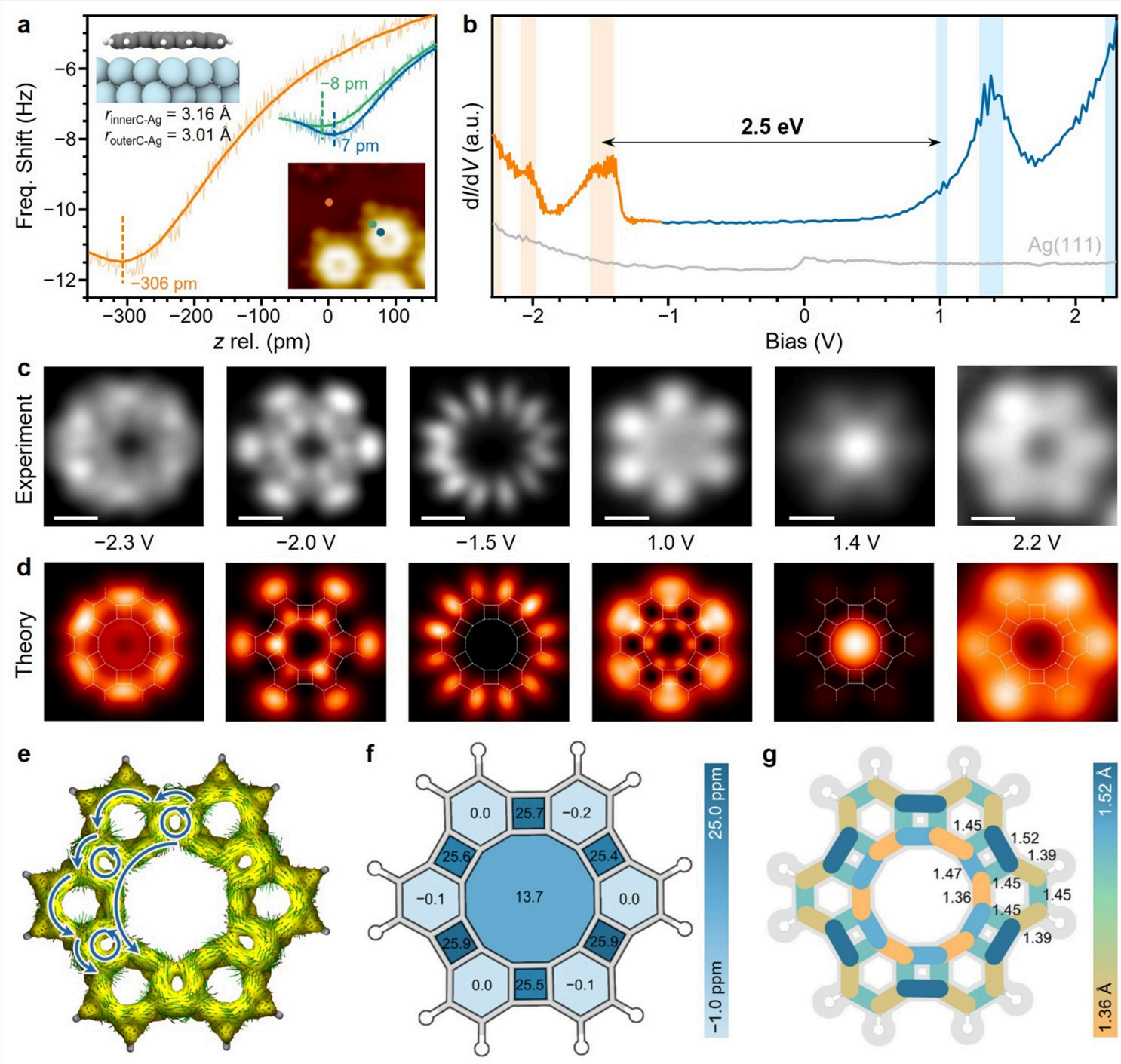

Figure 4

Surface adsorption, electronic structure, and aromaticity analyses of antiK on Ag(111). a, Δ*f*–*z* spectra (colored curves) measured at the inner and outer rings of antiK, and on the bare Ag(111) surface. Inset: Side view of the optimized geometric structure of an antiK molecule on Ag(111). **b**, Experimental d*I*/d*V*spectra acquired atop antiK (colored curves) and the bare Ag(111) surface (gray curve; onset of surface state: -60 mV). **c**,**d**, Experimental and simulated constant-height d*I*/d*V* maps of antiK acquired at the bias voltages resolved in the d*I*/d*V* spectrum. The simulated maps were derived from CASCI(12,12) natural orbitals (Supplementary Fig. 25). **e**, ACID analysis considering only the π-electron contributions. **f**, NICS plot with values calculated 1 Å above the centroid of each individual ring, along the normal to its respective ring plane, to account for the slight curvature of the molecular structure. The 1 Å distance was chosen to enhance sensitivity to the local π-electron system. **g**, Bond length distribution of antiK on the Ag(111) surface. All scale bars, 0.4 nm.

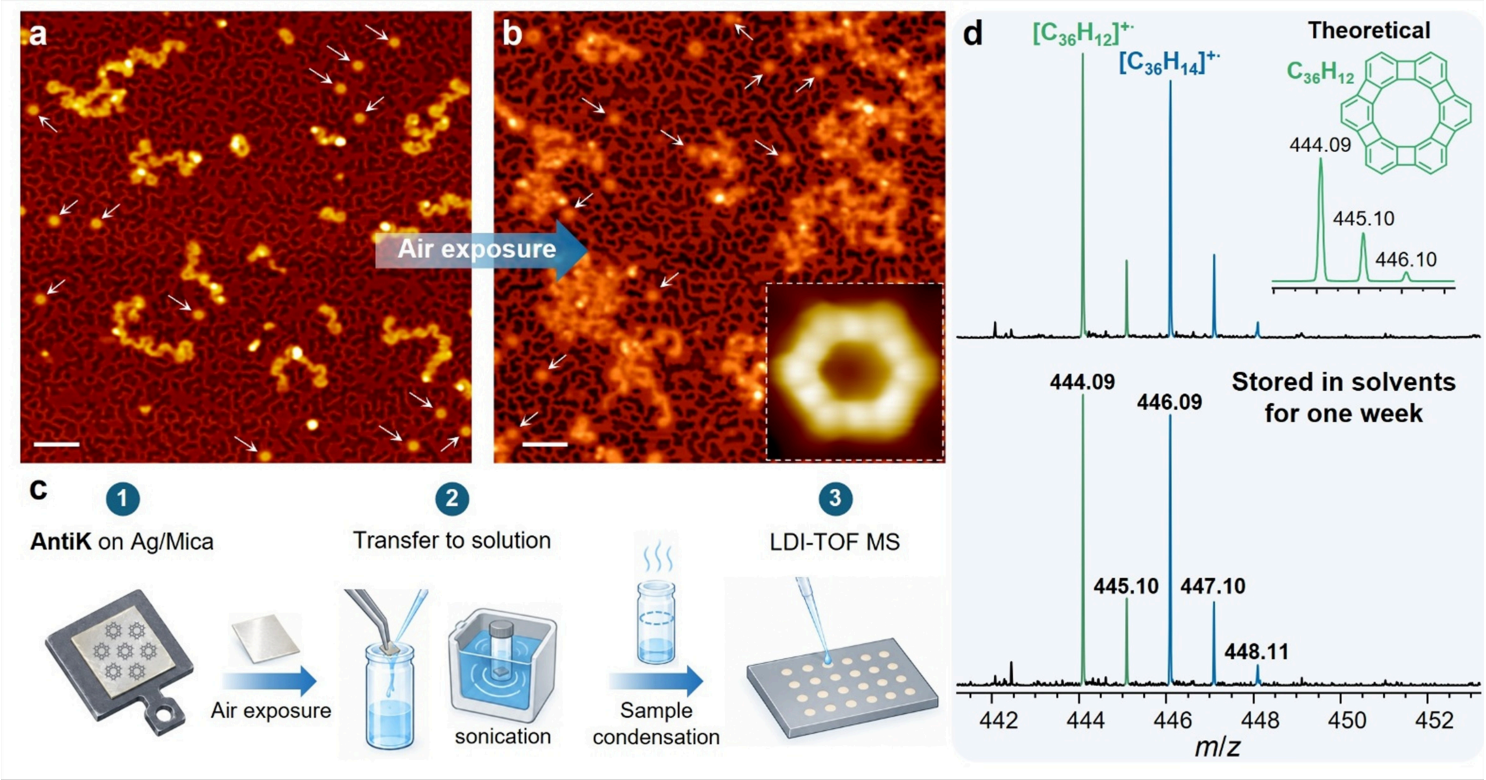

Figure 5

Stability test of antiK. a,**b**, STM images of the sample prepared by Br-mediated hot-surface deposition before (**a**) and after (**b**) ambient air exposure and annealing to 573 K. Intact antiK molecules are pointed by arrows, with their structural integrity confirmed by BR-STM shown in the bottom-right inset. **c**, Schematic illustration of the workflow for solvent extraction of surface-synthesized antiK and subsequent mass spectrometric analysis. **d**, LDI-MS spectra of surface-synthesized antiK extracted from Ag(111), acquired after a 4-hour pretreatment and after storage in solvents for one week. All scale bars: 5 nm.

Supplementary Files

This is a list of supplementary files associated with this preprint. Click to download.

- AntiKSINature.docx